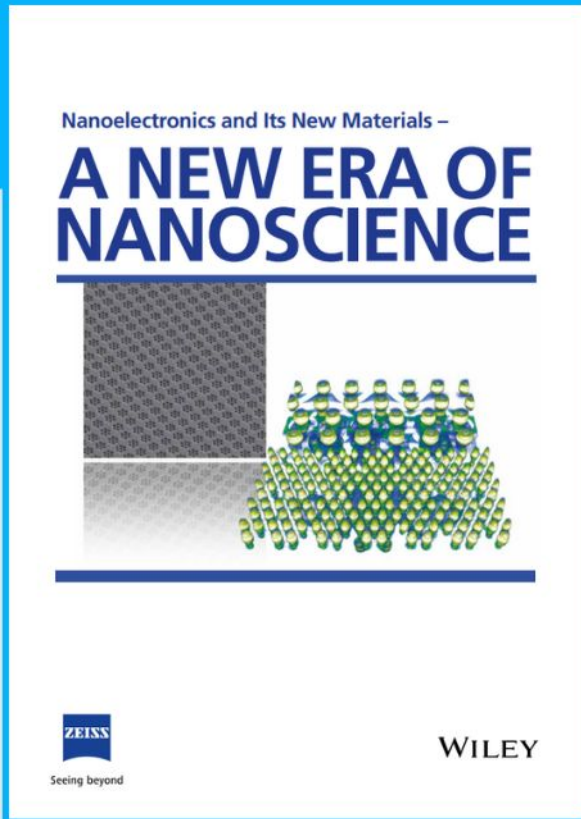




# Nanoelectronics and Its New Materials – A NEW ERA OF NANOSCIENCE



**Discover the recent advances in electronics research and fundamental nanoscience.**

Nanotechnology has become the driving force behind breakthroughs in engineering, materials science, physics, chemistry, and biological sciences. In this compendium, we delve into a wide range of novel applications that highlight recent advances in electronics research and fundamental nanoscience. From surface analysis and defect detection to tailored optical functionality and transparent nanowire electrodes, this eBook covers key topics that will revolutionize the future of electronics.

To get your hands on this valuable resource and unleash the power of nanotechnology, simply download the eBook now. Stay ahead of the curve and embrace the future of electronics with nanoscience as your guide.



Seeing beyond

**WILEY**

# Anti-Atherogenic Effect of Stem Cell Nanovesicles Targeting Disturbed Flow Sites


Jeong-Kee Yoon, Dae-Hyun Kim, Mi-Lan Kang, Hyeon-Ki Jang, Hyun-Ji Park, Jung Bok Lee, Se Won Yi, Hye-Seon Kim, Sewoom Baek, Dan Bi Park, Jin You, Seong-Deok Lee, Yoshitaka Sei, Song Ih Ahn, Young Min Shin, Chang Soo Kim, Sangsu Bae, YongTae Kim,\* and Hak-Joon Sung\*

Atherosclerosis development leads to irreversible cascades, highlighting the unmet need for improved methods of early diagnosis and prevention. Disturbed flow formation is one of the earliest atherogenic events, resulting in increased endothelial permeability and subsequent monocyte recruitment. Here, a mesenchymal stem cell (MSC)-derived nanovesicle (NV) that can target disturbed flow sites with the peptide GSPREYTSYMPH (PREY) (PMSC-NVs) is presented which is selected through phage display screening of a hundred million peptides. The PMSC-NVs are effectively produced from human MSCs (hMSCs) using plasmid DNA designed to functionalize the cell membrane with PREY. The potent anti-inflammatory and pro-endothelial recovery effects are confirmed, similar to those of hMSCs, employing mouse and porcine partial carotid artery ligation models as well as a microfluidic disturbed flow model with human carotid artery-derived endothelial cells. This nanoscale platform is expected to contribute to the development of new theragnostic strategies for preventing the progression of atherosclerosis.

## 1. Introduction

Atherosclerosis is a critical cause of mortality, but current diagnostic methods are not capable of detecting the early pathogenic signals associated with irreversible atherosclerosis cascades. Conventional preventative and therapeutic options are aimed at lowering cholesterol levels, blood pressure, or plaque formation, and are still widely used despite the substantial residual risk of disease progression. One of the earliest atherogenic events is the generation of disturbed blood flow, which occurs at the branch points, curved regions, or distal to stenosis,<sup>[1]</sup> and results in dysfunction of vascular endothelial cells (ECs).<sup>[2]</sup> Under normal blood flow, ECs are aligned with the blood flow direction and maintain their anti-inflammatory and anti-thrombogenic functions.<sup>[3]</sup> However,

Dr. J.-K. Yoon, Dr. D.-H. Kim, H.-S. Kim, S. Baek, D. B. Park, J. You, Dr. Y. M. Shin, Prof. H.-J. Sung  
Department of Medical Engineering  
Yonsei University College of Medicine  
Seoul 03722, Republic of Korea  
E-mail: hj72sung@yuhs.ac  
Dr. M.-L. Kang, Dr. S. W. Yi  
TMD LAB Co., Ltd  
Department of Medical Engineering  
Yonsei University College of Medicine  
Seoul 03722, Republic of Korea  
Dr. H.-K. Jang, Prof. S. Bae  
Department of Chemistry, Research Institute for Convergence  
of Basic Sciences  
Hanyang University  
Seoul 04763, Republic of Korea

 The ORCID identification number(s) for the author(s) of this article can be found under <https://doi.org/10.1002/smll.202000012>.

© 2020 The Authors. Published by WILEY-VCH Verlag GmbH & Co. KGaA, Weinheim. This is an open access article under the terms of the Creative Commons Attribution License, which permits use, distribution and reproduction in any medium, provided the original work is properly cited.

DOI: 10.1002/smll.202000012

Dr. H.-J. Park  
George W. Woodruff School of Mechanical Engineering  
Georgia Institute of Technology  
Atlanta, Georgia 30313, USA  
Prof. J. B. Lee  
Department of Biological Science  
Sookmyung Women's University  
Seoul 04310, Republic of Korea  
S.-D. Lee, Dr. C. S. Kim  
Numais Co., Ltd  
Seoul 03722, Republic of Korea  
Dr. Y. Sei, Dr. S. I. Ahn  
George W. Woodruff School of Mechanical Engineering  
Parker H. Petit Institute for Bioengineering and Bioscience  
Georgia Institute of Technology  
Atlanta, Georgia 30313, USA  
Prof. Y. Kim  
George W. Woodruff School of Mechanical Engineering  
Wallace H. Coulter Department of Biomedical Engineering  
Parker H. Petit Institute for Bioengineering and Bioscience (IBB)  
Institute for Electronics and Nanotechnology (IEN)  
Georgia Institute of Technology  
Atlanta, Georgia 30313, USA  
E-mail: ytkim@gatech.edu

under atheroprone, or disturbed, flow, EC functions are blocked with increased inflammatory and thrombotic events, ultimately leading to atherosclerosis.<sup>[4]</sup> Therefore, the theragnostic targeting of disturbed flow sites may serve as a promising solution in treating or preventing this fatal chronic disease; however, this strategy has not yet been thoroughly demonstrated.

Mesenchymal stem cells (MSCs) hold therapeutic promise for anti-atherosclerosis treatment<sup>[5]</sup> by regulating immune responses and attenuating the proliferation of vascular smooth muscle cells (VSMCs).<sup>[5b,c]</sup> However, their poor survival rate and deficient targeting efficiency remain the major limitations of MSCs for clinical translation. MSC-derived exosomes have emerged as therapeutic nanocarriers with a prolonged circulation time that promote cellular interactions<sup>[6]</sup> while retaining the cell-originated anti-inflammatory and pro-regenerative properties. Despite attempts to develop exosome-based therapeutics for several fatal diseases and injuries, including cardiovascular disease,<sup>[7]</sup> kidney injury,<sup>[8]</sup> liver diseases,<sup>[9]</sup> and neurological diseases,<sup>[10]</sup> controlling the size uniformity and content identity with a high yield throughout the long-term, laborious production processes is a significant challenge to be overcome. A recent alternative engineering approach enabled a 100-fold increase in the high-yield production of cell-derived nanovesicles (NVs) by physically breaking down the cells through micropore filtration steps, and inducing the self-assembly of the resulting cell membrane components and internal contents.<sup>[11]</sup>

In the present study, we developed human MSC-derived NVs that are functionalized with GSPREYTSYMPH (PREY), a disturbed flow-targeting peptide that was previously identified from the *in vivo* phage display screening of a hundred million candidates (Figure S1, Supporting Information).<sup>[12]</sup> We used plasmid DNA that was designed to specifically functionalize the MSC membrane with PREY and produced NVs through physical cell crushing and subsequent self-assembly. Here, we demonstrate the effective anti-inflammatory and pro-endothelial recovery effects of these PREY-expressing MSC (PMSC)-NVs targeting disturbed flow regions in mouse and porcine partial carotid artery ligation (PCL) models. We further confirmed these effects using a microfluidic disturbed flow model with human coronary artery-driven endothelial cells (hCAECs). Thus, this nanotechnology-based targeted treatment of endothelial inflammation shows potential to promote the development of theragnostic strategies for preventing and treating atherosclerosis.

## 2. Results

### 2.1. Outward PREY Display on the Membrane

To enable NVs to target disturbed flow sites, the targeting peptide, PREY, was displayed outward by expressing a specifically designed plasmid throughout the MSC membrane (PMSCs). Specifically, the plasmid was designed to express the PREY-extracellular domain with a signal peptide at the N-terminus so that the signal peptide could guide the outward localization of the PREY-extracellular domain from the MSC membrane and undergo cleavage to deactivate the guiding signal. Furthermore, the ability of three transmembrane proteins (TMPs), that is,

the exosome marker (CD86) and MSC markers (CD105 and CD271), to improve PREY expression was evaluated. In this way, PREY's ability to navigate and target disturbed flow sites was maximized. PREY was linked with a v5 tag and then with green fluorescent protein (GFP) (outward N-terminal-promoter-signal peptide-PREY-v5 tag-TMP-GFP-inward C-terminal) to identify the localization and expression levels of PREY outside and inside the cell membrane, respectively (Figure 1A; Figure S2, Supporting Information).

Among the test groups with the three TMPs, the expression level of nerve growth factor receptor (NGFR) with PREY-CD271 was higher than that obtained with either PREY-CD86 or PREY-CD105 in both adipose-derived stem cells (ASCs) and bone marrow-derived stem cells (BMSCs), indicating its superior transfection efficiency (Figure 1B; Figure S3A, Supporting Information). When the dose of PREY-CD271 plasmid was increased, the NGFR expression level increased in a dose-dependent manner, while cell viability drastically decreased after transfection of the 2× dose (Figure 1C; Figures S3B and S3C, Supporting Information). Hence, the optimal plasmid dose was determined as 1× (1 μg PREY-plasmid per 1 × 10<sup>6</sup> cells) considering the balance with cell viability. Moreover, annexin V<sup>+</sup> staining showed more viable ASCs than BMSCs post-transfection, indicating ASCs as a more suitable source for PREY transfection (Figure 1C).

To verify the outward display of PREY on the MSC membrane, a v5 tag was immunostained as it was placed next to PREY in the sequence (outward N-terminal-promoter-signal peptide-PREY-V5-TMP-GFP-inward C-terminal). Both the adhered (Figure S4, Supporting Information) and suspended (Figure 1D; Video S1, Supporting Information) forms of PMSCs were used to determine the expression level and location of PREY, respectively, as neither form was sufficient on its own to obtain both information types clearly. In the adherent form, PREY was highly expressed along the cell membrane as evidenced by the v5 tag and GFP signals, indicating successful transfection. Confocal images of the suspended form (in which cells were embedded in a gelatin hydrogel) showed the appearance of v5 tag (red) and GFP (green) signals outside and inside the MSC membrane boundary, respectively, verifying outward PREY display on the cell membrane. The image was generated by confocal microscopy with z-stacking from top view to downstream focal planes. Therefore, the red V5 tag signals showed up not only outside the membrane (down-stream focal planes) but also in the cytosol slightly (top view). However, the red V5 tag signals showed up outside the membrane dominantly.

### 2.2. Extrusion and Characterization of NVs

To produce PMSC-NVs, PMSCs were sequentially extruded using ACSs through a series of polycarbonate micropore membranes with gradually decreasing pore diameters from 10, 5, and finally 0.4 μm (Figure S1B, Supporting Information). Transmission electron microscopy (TEM) (Figure 1E) showed uniform distributions of PMSC-NV diameters with an average of 472 ± 12.1 nm. The NV extrusion process was mediated by the surface tension of the polycarbonate filter in collaboration with static friction to the filter and the piston rubber, which



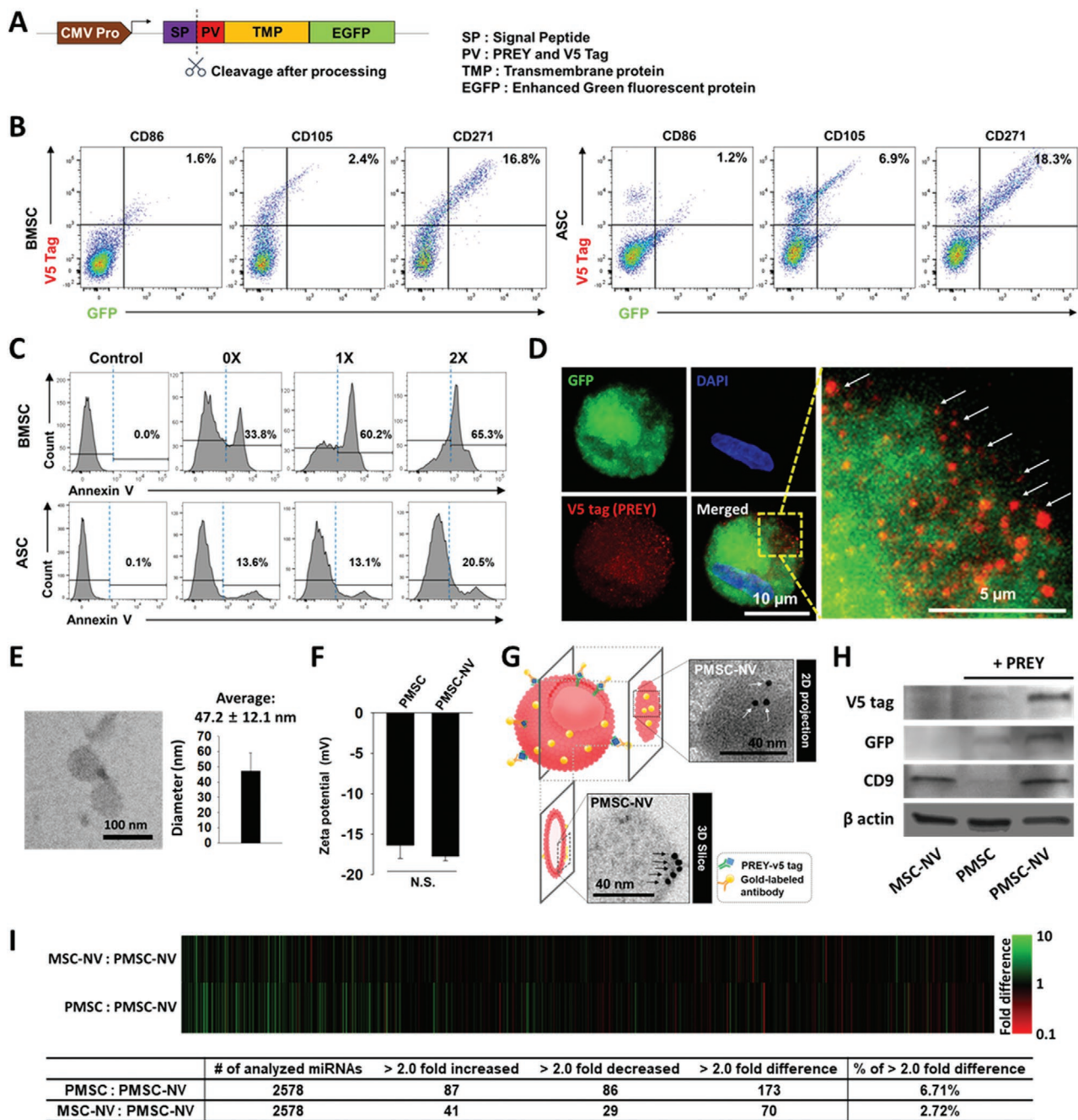


**Figure 1.** Preparation and characterization of PMSC-NVs. A) Schematic diagram of the plasmid design to express PREY on the outer layer of the MSC membrane. GFP (internal membrane signal)-transmembrane protein-v5 tag (outer membrane signal)-PREY was designed to validate the expression and localization of PREY. B) Transfection efficiency quantitatively compared by flow cytometry (*x*-axis: GFP<sup>+</sup> cells/*y*-axis: V5 tag<sup>+</sup> cells) in two paired hMSC types (ASCs and BMSCs) with three transmembrane proteins (CD86, CD105, and CD271). The CD271-ASC pair was pre-selected because it had the highest transfection efficiency. C) PREY-CD271 plasmid dose-dependent apoptosis (0x: electroporation without plasmid and 1x, 2x: 100, 200 ng plasmid per 10<sup>5</sup> cells) evaluated using Alexa Fluor 488-conjugated annexin V at 30 min post-transfection. Given the higher cell viability, ASCs were used to produce NVs for subsequent experiments. D) Localization of GFP (green internal membrane signal) and PREY-v5 tag (red outer membrane signal) visualized in PMSCs. The red and green signals in the merged z-stack confocal image were dominantly observed outside and inside the membrane, respectively. White arrows indicate v5 tag signals outside the cell membrane with internal GFP signals (blue: nucleus with DAPI staining). Scale bar = 10 or 5 μm. E) Morphology and size distribution of PMSC-NVs evaluated using TEM. Scale bar = 100 nm. The outward display of PREY was confirmed using F) zeta potential (N.S. = no significant difference between the comparison groups) and G) TEM imaging by immunostaining of PREY-v5 tag using a gold nanoparticle-labeled antibody. The schematic illustration shows the imaging directions of TEM because the images were produced as a 2D projection or 3D slice view. White (top 2D projection view) and black (intracellular 3D slice view) arrows indicate gold nanoparticle locations and thereby confirm outward display of the PREY-v5 tag on the PMSC-NV surface. Scale bar = 40 nm. Preservation of the H) transfected components and I) internal miRNA components analyzed using western blotting and miRNA array, respectively (*n* = 3). The PMSC-NV production process did not alter the cellular components.

was considered to be the main reason for the generation of small NV sizes as reported previously.<sup>[13]</sup> The outward display of PREY with an intact membrane structure maintained before and after NV formation was further confirmed based on the non-significantly different zeta-potentials between the PMSCs and PMSC-NVs (Figure 1F), as well as TEM imaging of the outward v5 tag projection from the NV membrane stained with a gold-conjugated antibody (Figure 1G). In addition, the intact preservation of the PREY-peptide (GFP and v5 tag) and exosome characteristics (CD9) during transfection and NV extrusion were confirmed by western blot analysis (Figure 1H; Figure S5, Supporting Information). Since a series of decremental size filters were used to produce PMSC-NVs, large size proteins (e.g., big intracellular organelles) might be filtered out from PMSCs while maintaining the membrane characteristics. As a result, relatively more PREY peptides appeared to be loaded in the total amount of PMSC-NV lysate for electrophoresis and thereby to generate the darker bands compared to the bands of PMSC group.

Next, we compared the intracellular components in MSC-NVs, PMSCs, and PMSC-NVs to confirm their preservation after PREY transfection and NV extrusion. MicroRNAs (miRNAs) have recently emerged as important,<sup>[14]</sup> and a majority of them are transported via exosomes.<sup>[15]</sup> As NVs are inherently similar to exosomes, the miRNA content of PMSC-NVs, MSC-NVs, and PMSCs was profiled by miRNA array (Figure 1I; Tables S1 and S2, Supporting Information). The transfection (MSC-NV vs PMSC-NV) and extrusion (PMSC vs PMSC-NV) processes altered the miRNA expression levels by more than twofold only for 2.72% and 6.71% of the total miRNAs, respectively, proving the overall preservation of the intracellular content during their production (Figure 1I). Among the anti-atherogenic miRNAs, the levels of miR-21, miR-132, miR-10, miR-146, miR-143, and let-7 increased during the extrusion, while the expression levels of other miRNAs were retained during NV production from ASCs (Tables S1 and S2, Supporting Information).

### 2.3. In Vitro Anti-Inflammatory Effects of MSC-NVs

MSCs and MSC-derived intracellular contents are well known to exert potent anti-inflammatory effects.<sup>[5]</sup> Hence, the anti-inflammatory effects (Figure 2A) of BMSC-NVs, ASC-NVs, and PMSC-NVs were examined. In particular, since our previous study reported that monocyte/macrophage could uptake PREY-liposome,<sup>[12]</sup> mouse bone marrow-derived macrophages (BMDMs) obtained after primary culture or the mouse macrophage cell line (Raw 246.7) were treated with the MSC-NVs to inhibit their inflammatory responses. First, the effective cellular uptake of the MSC-NVs (ASC-NVs, BMSC-NVs, and PMSC-NVs) by the activated BMDMs was confirmed by visualization with DiI and DiO, respectively (Figure 2B).

Second, the anti-inflammatory activities of BMSC-NVs, ASC-NVs, and PMSC-NVs on mouse macrophages were examined by quantitative reverse transcription-polymerase chain reaction (qRT-PCR) analysis. Lipopolysaccharide (LPS) treatment induced expression of both anti- and pro-inflammatory cytokines in the mouse macrophage cell line RAW264.7 (Figure S6, Supporting Information). However, when LPS-activated BMDMs

were treated with the test NVs (Figure 2C), the mRNA expression levels of the anti-inflammatory cytokines interleukin (IL)-10 and IL-13 were increased, while those of the pro-inflammatory cytokines IL-1 $\beta$  and tumor necrosis factor (TNF)- $\alpha$  were not, indicating maintenance of the anti-inflammatory potential of the macrophages by MSC-NVs even post-extrusion from MSCs. To prove that this response is not specific to primary cultured BMDMs, the mouse macrophage cell line Raw264.7 was used to conduct dot blot assays with the conditioned post-culture media, followed by similar quantitative analyses of the secreted cytokines and chemokines. The results supported the significant decreases in pro-inflammatory activities (Figure 2D) following the treatment of all test NV groups along with significant reduction in the phagocytic activities against the bacteria component (Figure 2E upper row). Oil red O staining to detect the uptake of oxidized low-density lipoprotein (ox-LDL; Figure 2E lower row) also confirmed the significant reduction of phagocytic activities by the treatment of all MSC-NV groups except for the BMSC-NV group, indicating an inhibitory effect of ASC-NV and PMSC-NV on the foam cell formation of macrophages. Again, there was no significant difference in these anti-inflammatory effects among the three test NV groups. Foam cell formation of macrophages resulting from the uptake of ox-LDL is a critical event in atherosclerosis development, which induces phenotype changes and the intimal ingrowth of VSMCs.<sup>[16]</sup> Therefore, these results indicate that MSC-NVs have potential to prevent this atherogenic process.

### 2.4. In Vitro Pro-EC Recovery Effect of MSC-NVs

The EC-recovery effects of MSC-NV treatment (Figure 3A) were examined by activating the pro-inflammatory dysfunctions of immortalized mouse aortic endothelial cells (iMAECs) with LPS. Effective internalization of ASC-NVs, BMSC-NVs, and PMSC-NVs into activated iMAECs was visualized by labeling with DiO and DiI, respectively (Figure 3B); there were no visually detectable differences in the NV uptake among the test NV groups. ECs dominantly express E-selectin, intercellular adhesion molecule 1 (ICAM-1), and vascular cell adhesion molecule 1 (VCAM-1) to recruit inflammatory cells upon their dysfunctional activation. Indeed, qRT-PCR (Figure 3C) showed that the mRNA expression levels of these markers in iMAECs were all increased by LPS treatment,<sup>[17]</sup> but were significantly reduced to the level of saline group by treatment with either of the MSC-NVs types, indicating effective induction of EC dysfunction by 100 ng mL<sup>-1</sup> of LPS as well as a promising EC-recovery effect of all MSC-NV types. We further confirmed this result by immunostaining for VCAM-1 protein expression (Figure 3D) because VCAM-1 is one of the earliest endothelial dysfunction markers.<sup>[18]</sup> Moreover, this pro-EC recovery effect was not significantly different among ASC-NVs, BMSC-NVs, and PMSC-NVs, indicating that PREY transfection did not impair the therapeutic effect of MSC-NVs.

Cyclosporin A (CyA) treatment is known to disrupt tubular formation by inhibiting angiogenic EC activities.<sup>[19]</sup> Thus, the pro-angiogenic (Figure S7, Supporting Information) and pro-EC recovery (Figure 3E) effects of BMSC-, ASC-, and PMSC-NVs were examined by culturing human umbilical vein endothelial cells

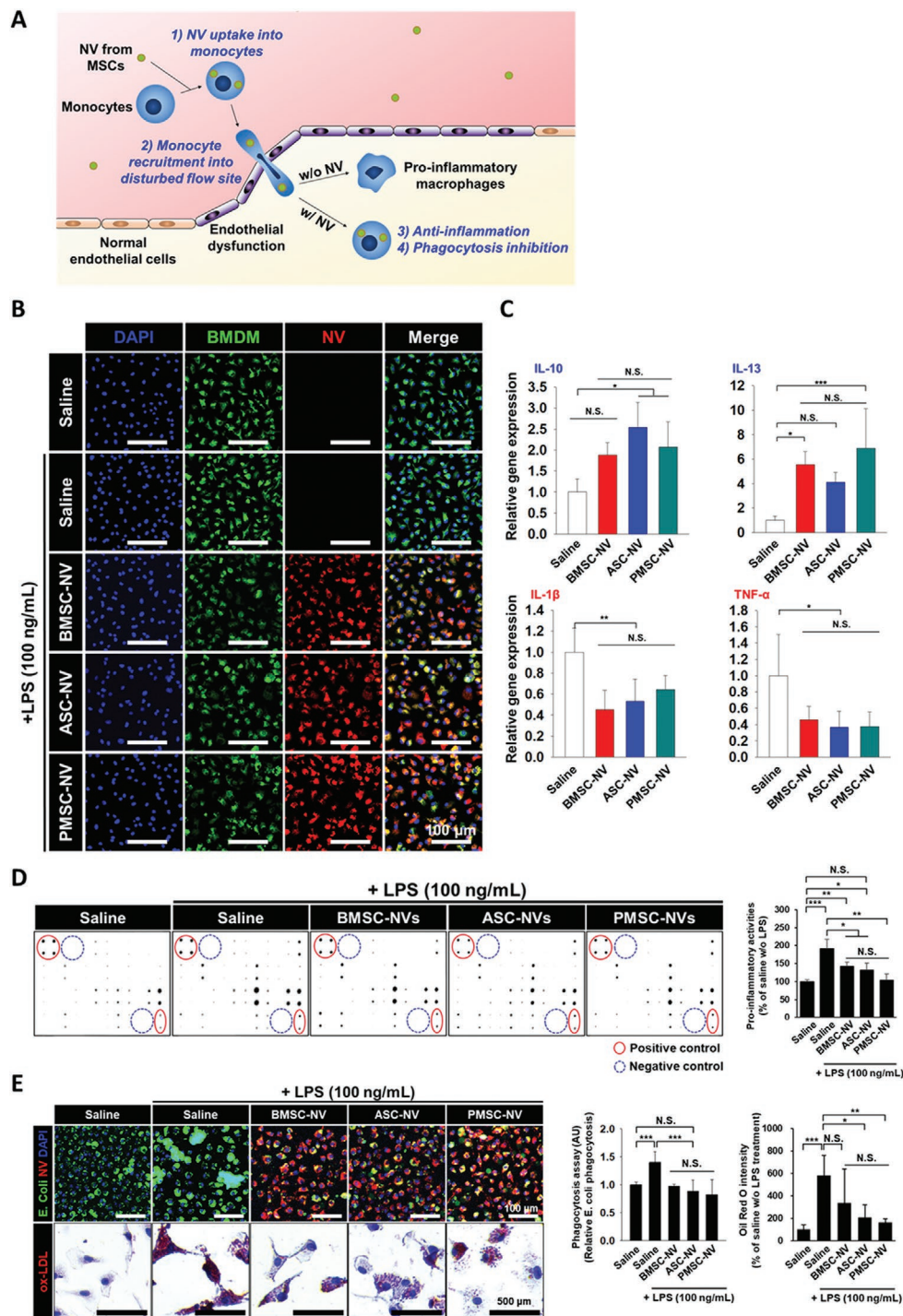


**Figure 2.** Anti-inflammatory effects of activated monocytes/macrophages following treatment with MSC-NVs derived from BMSCs (BMSC-NVs), ASCs (ASC-NVs), or PMSCs (PREY-transfected ASCs). **A**) Monocytes uptake of MSC-NVs for anti-inflammation and phagocytosis inhibition. **B**) BMDMs and NVs visualized using DiO (green) and Dil (red), respectively (blue: nucleus with DAPI staining). All test NV types were internalized efficiently into BMDMs. Scale bar = 100  $\mu$ m. **C**) mRNA expression of anti-inflammatory (IL-10 and IL-13) and pro-inflammatory markers (IL-1 $\beta$  and TNF- $\alpha$ ) in BMDMs determined by qRT-PCR. **D**) Dot blot assays using conditioned post-culture media of mouse macrophages (Raw 264.7). The darkness of each dot corresponds to the amount of pro-inflammatory cytokine or chemokine in the test media with corresponding quantitative analysis (right graph). Pro-inflammatory activities were reduced by all test NV groups. **E**) Phagocytic activities of the test groups determined by measuring the amount of internalized *Escherichia coli* particles (upper panel) and by Oil Red O staining of ox-LDL (lower panel), which were also reduced in all test NV groups except for the ox-LDL uptake of the BMSC-NV group. There was no significant difference among the three MSC-NV types. Scale bars = 100  $\mu$ m (upper panel) and 500  $\mu$ m (lower panel). \* $p$  < 0.05, \*\* $p$  < 0.01, and \*\*\* $p$  < 0.001 between/among the comparison groups. N.S. indicates no significant difference between/among the comparison groups.



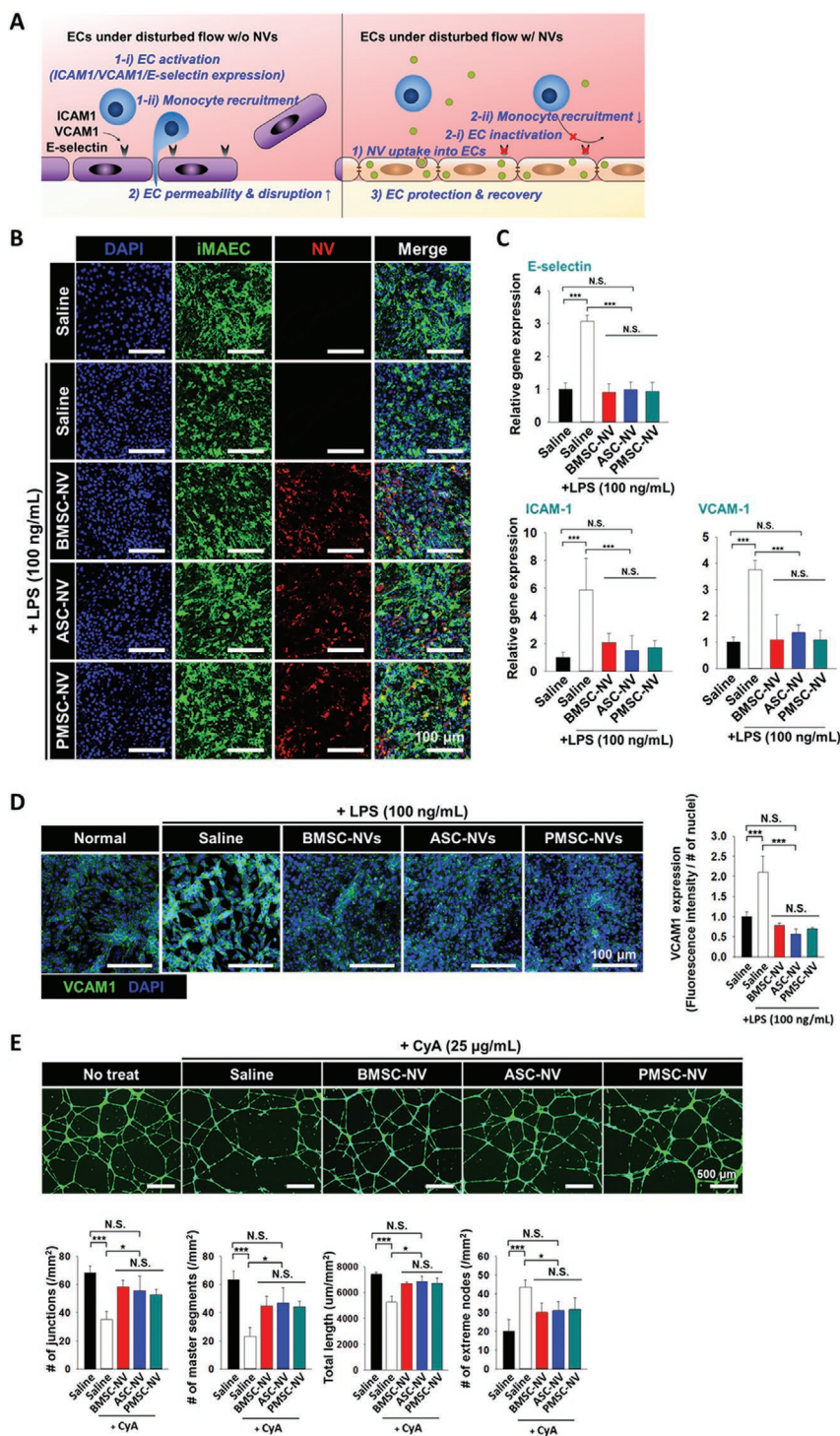


**Figure 3.** Vascular protective effects of ECs due to treatment with MSC-NVs derived from BMSCs (BMSC-NVs), ASCs (ASC-NVs), or PMSCs (PREY-transfected ASCs). A) EC dysfunction was recovered by MSC-NV uptake, as MSC-NV provided EC protection and inhibited monocyte recruitment. B) iMAECs and MSC-NVs were visualized using DiO (green) and Dil (red), respectively (blue: nucleus with DAPI staining). All MSC-NV types were internalized efficiently into iMAECs. Scale bar = 100 μm. C) Gene expression of EC dysfunction markers (E-selectin, ICAM-1, and VCAM-1) was measured by qRT-PCR, which was also reduced by treatment of all MSC-NV types. D) Protein expression of VCAM-1 (green) in iMAECs was determined with quantification by immunostaining (blue: nucleus with DAPI staining). Scale bars = 100 μm. E) Disruption of EC tube formation was induced by cyclosporin A (CyA) treatment. The images and their quantification results show the vascular protective effect of all types of MSC-NV treatment, but there was no significant difference between/among the MSC-NV types. Scale bars = 500 μm. \* $p < 0.05$  and \*\*\* $p < 0.001$  between/among the comparison groups. N.S. indicates no significant difference between/among the comparison groups.

(HUVECs) on Matrigel, followed by co-treatment with CyA and NVs at 2 h (Figure S7, Supporting Information) or 12 h (Figure 3E) post-seeding. Tube structural factors (i.e., junction, master segments, total length, and extreme node number) of HUVECs were then determined. As a result, the MSC-NV treatment enhanced the pro-EC recovery and pro-angiogenic effects of HUVECs in response to CyA treatment regardless of the MSC source.

## 2.5. In Vivo Targeting and Anti-Atherogenic Functions

The theragnostic efficiency of PMSC-NVs was determined in a mouse PCL model established by ligation of the external carotid artery (ECA), internal carotid artery (ICA), occipital artery (OA), three of the four left carotid artery (LCA) branches (Figure S8, Supporting Information), and formation of disturbed blood flow was confirmed by Doppler ultrasound imaging (Figure S9, Supporting Information). MSC-NVs, PMSC-NVs, and PMSCs were then intravenously injected through the tail vein on day 3 post-ligation. An *in vivo* imaging system (IVIS) was used to visualize their biodistribution at 24 h post-injection (Figure 4A,B; Figure S10, Supporting Information). Since we previously demonstrated that a scrambled peptide of the PREY sequence had no significant targeting effect,<sup>[12]</sup> no peptide control group was included in this study. The LCA-targeting efficiency of PMSC-NVs was better than that of MSC-NVs or PMSCs, indicating the synergistic roles of PREY and NV to hinder the pulmonary capillary entrapment of cells and thereby to effectively target disturbed flow sites. Pulmonary capillary entrapment is a major obstacle for systemic cell delivery.<sup>[20]</sup> Our previous proteomic analysis<sup>[12]</sup> identified filamin A as a target molecule of PREY. Immunostaining of the unligated RCAs and ligated LCAs at 24 h post injection (Figure 4C) showed that filamin A expression was significantly higher in the LCAs than in the RCAs, confirming its overexpression at the disturbed flow site for PMSC recruitment. Among the test groups in which NVs were labeled with Vivotrack 680, only PMSC-NVs clearly co-localized with filamin A.

Given the demonstrated anti-inflammatory and pro-EC recovery effects (Figures 2 and 3) of MSC-NVs as well as the targeting efficiency of PREY (Figure 4A–C), we hypothesized that their combination (PMSC-NVs) would exert synergistic theragnostic effects that could prevent the early progression of atherosclerosis. To test this possibility, we established the same PCL model using ApoE knockout (KO) mice because this mouse strain showed more aggressive atherosclerosis development compared to the corresponding wild-type strain (Figure S11, Supporting Information). H&E and Masson's trichrome staining of LCAs and RCAs harvested at day 11 post NV injection from the ApoE KO PCL model showed that the PMSC-NVs effectively prevented neointima formation and aggressive inflammatory responses with maintenance of the normal control-like vessel morphology, whereas the other test groups did not show clear anti-inflammatory therapeutic effects (Figure 4D). Moreover, PMSCs alone could not efficiently prevent neointima formation compared to PMSC-NVs (Figure S12, Supporting Information), which is likely because the dose was too low to allow for efficient targeting. Protein expression levels of CD68 (Figure 4D) and VCAM-1 (Figure 4F) were further determined as indications of monocyte recruitment and

EC activation<sup>[18]</sup>, respectively. After treatment with PMSC-NVs, these expression levels decreased to those of the controls with no visible toxic effects on the heart, lung, liver, and spleen post systemic circulation (Figure S13, Supporting Information). In contrast, the other test groups exhibited significantly higher expression levels of these markers compared to those of the normal control and PMSC-NV groups.

## 2.6. In Vivo Porcine PCL and In Vitro Human EC Models

As a pre-clinical, large animal model, we next established a porcine PCL model to confirm the targeting efficiency of PMSC-NVs with regard to disturbed blood flow sites according to a previously established method.<sup>[21]</sup> In brief, a stainless-steel rod (diameter = 0.9 mm) was tightly ligated with the LCA (diameter = 4.5 mm) and then removed (Figure 5A top), leading to 70–80% occlusion of the LCA (Figure 5A bottom). Clear disturbance of flow in the distal part of the ligated LCA was confirmed by Doppler ultrasound imaging (Figure 5B; Video S2, Supporting Information). Furthermore, filamin A was highly expressed on the endothelium of the ligated LCA compared to that detected on the untreated RCA (Figure 5C). Vivotrack680-labeled MSC-NVs or PMSC-NVs were intravenously administered through an ear vein and systemically circulated on day 3 post-ligation. The RCA, LCA, and aortic arches were harvested from normal, induced disturbed, and naturally disturbed flow sites, respectively, at 24 h or 21 days after NVs injection. Natural disturbed flow occurs in an aortic arch due to its curvature and branch structures.<sup>[22]</sup> The IVIS images demonstrated that more PMSC-NVs accumulated in the region distal to the ligation point of the LCA, which indicated pathogenic remodeling,<sup>[23]</sup> which was not observed in the RCA (Figure 5D; Figure S14A, Supporting Information). In the aortic arch samples, the IVIS fluorescence distribution of PMSC-NVs was more highly correlated with the disturbed flow sites compared to that of MSC-NVs, indicating the effective targeting function of PREY (Figure 5F; Figure S14B, Supporting Information), which was further supported by the greater co-localization of CD31 with PMSC-NVs than with MSC-NVs (Figure 5E,G).

Finally, we examined the efficiency of PMSC-NV to target hCAECs (Figure 6) and human aortic ECs (hAECs; Figure S15, Supporting Information) under disturbed flow using an *in vitro* microfluidic model. The EC monolayer attached to a collagen-coated glass surface was exposed to medium flow generated by the pumping system, which successfully mimics blood flow under either healthy or atherogenic conditions. Moreover, this microfluidic system enables precise observations of the targeting site as well as the targeting efficiency of PMSC-NVs, which is challenging to achieve with *in vivo* experiments. To mimic healthy and atherogenic conditions in the blood vessels, the ECs were exposed to either normal (10 dyne cm<sup>-2</sup>) or disturbed (10 and -9 dyne cm<sup>-2</sup> with a 1 Hz pulse) flow prior to NV treatment (Figure 6A–C). We confirmed that ECs exposed to normal flow were aligned with the flow direction, whereas this was not the case for those exposed to disturbed flow (Figure 6D). Moreover, the filamin A expression level increased under disturbed flow, while F-actin expression was similar between ECs exposed to normal and disturbed flows (Figure 6E). More importantly, the microfluidic model revealed



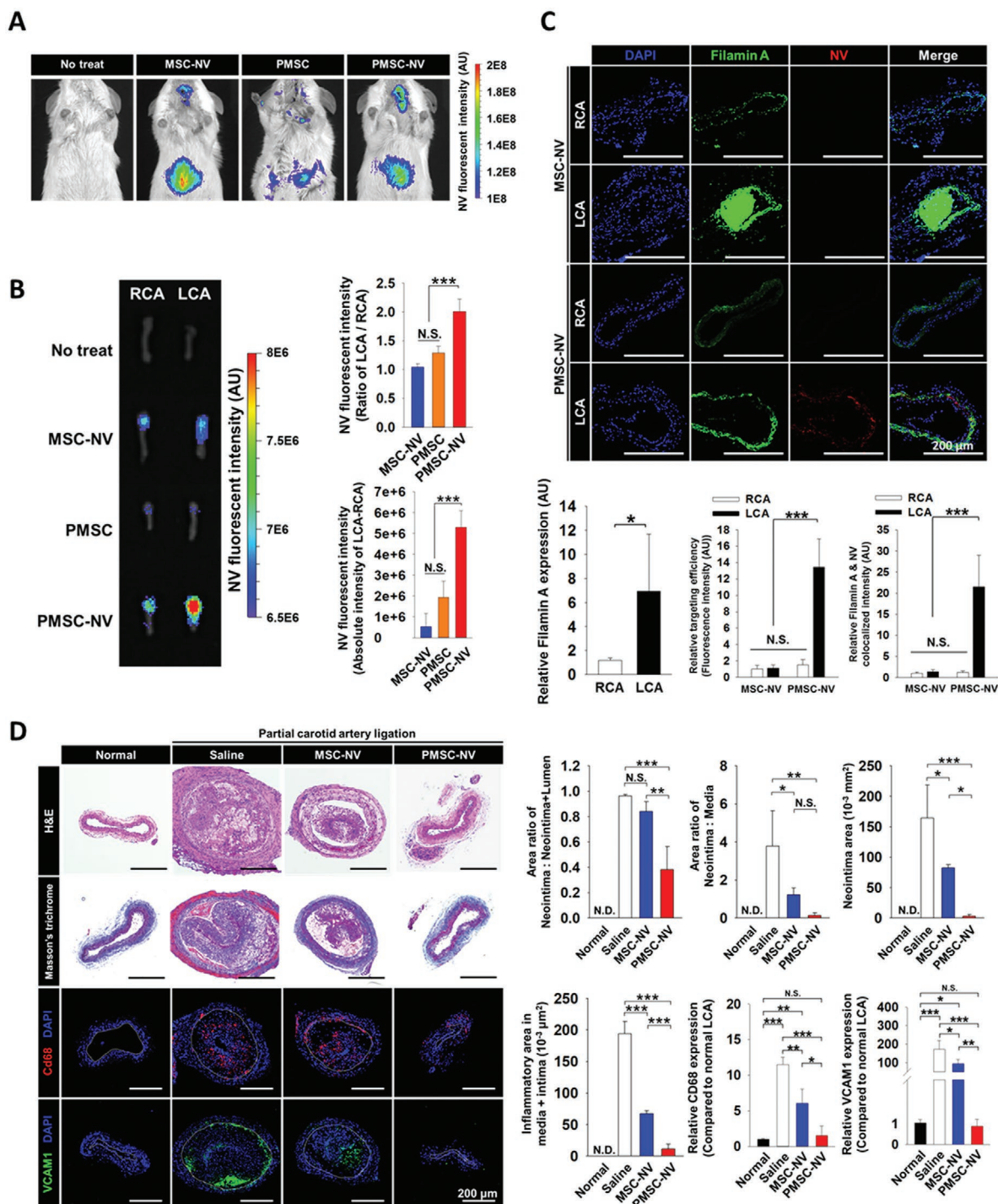


**Figure 4.** Theragnostic effect of PMSC-NVs on disturbed blood flow sites in the mouse model of partial carotid artery ligation (PCL). Vivotrack680-labeled MSC-NVs and PMSC-NVs were intravenously administered for systemic circulation on day 3 after PCL surgery. Vessels were harvested and analyzed at 24 h post-injection. Biodistribution was determined by an in vivo imaging system (IVIS) in A) the whole mouse body, and in B) the harvested RCA (control) and LCA (ligated) with quantitative comparison among MSC-NVs, PMSC-NVs, and PMSCs. C) Expression and co-localization of filamin A (green) protein with PMSC-NVs (red) were determined in the harvested RCA and LCA by immunostaining with quantitative analysis (blue: nucleus with DAPI staining). Scale bars = 200  $\mu$ m. D) H&E images (top row) of the LCA were obtained on day 14 after PCL surgery with quantitative analysis of neointimal structure parameters, indicating suppression of neointimal formation by PMSC-NV treatment. Inflammatory areas in harvested LCAs were detected by Masson's trichrome staining (second row) with quantitative analyses. Macrophage recruitment by ECs was determined with immunostaining of CD68 (third row) and VCAM-1 (bottom row) in the harvested LCA (blue: nucleus with DAPI staining). White lines indicate the inner boundary of the media layer facing the intima. Scale bars = 200  $\mu$ m. \* $p$  < 0.05, \*\* $p$  < 0.01, and \*\*\* $p$  < 0.001 between/among the comparison groups. N.S. indicates no significant difference between/among the comparison groups. N.D. indicates non-detectable.

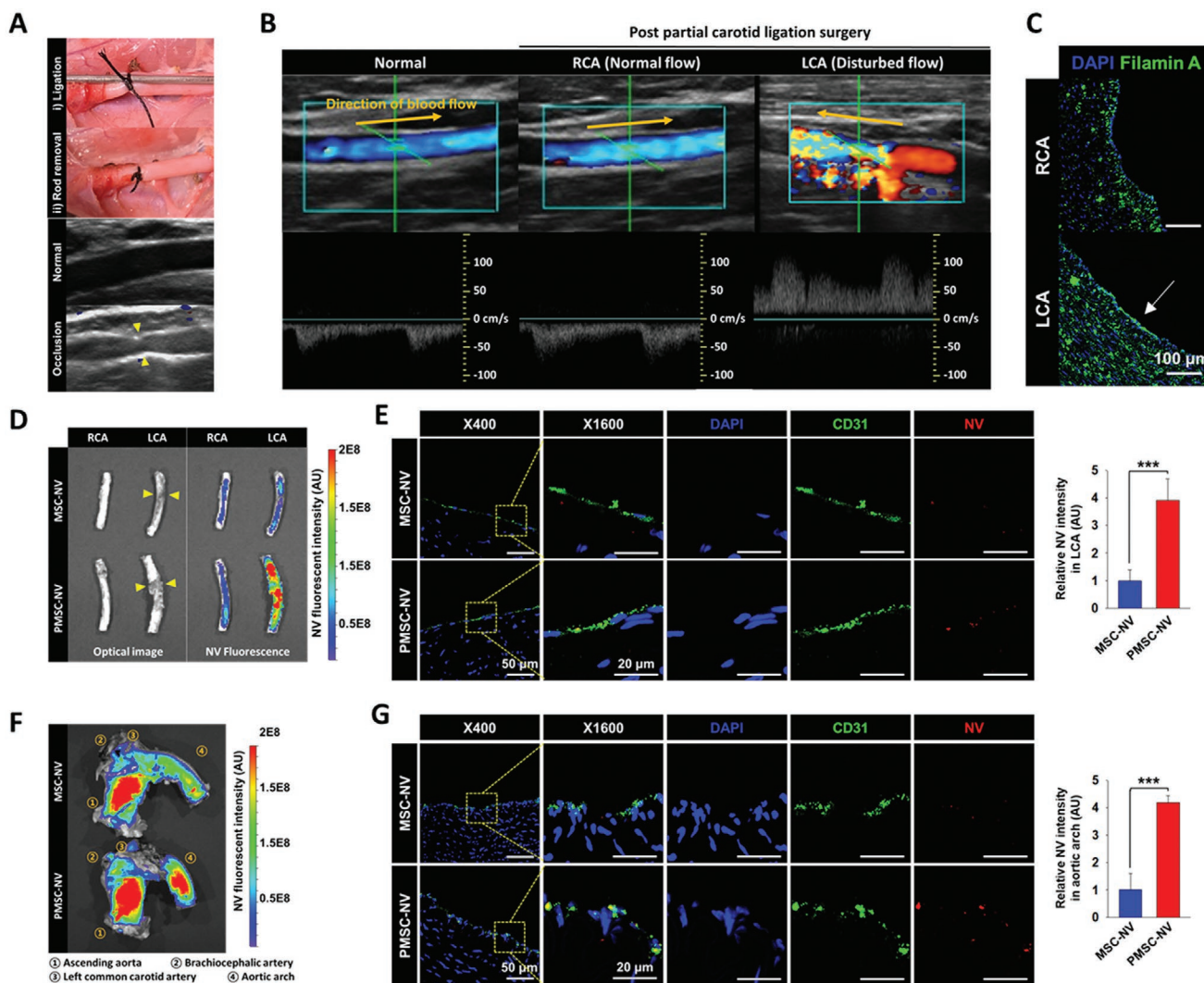


**Figure 5.** Efficiency of PMSC-NV targeting of disturbed flow sites in the porcine PCL model. A) The surgical ligation procedure of the LCA to induce a porcine PCL model using a stainless-steel rod (diameter = 0.9 mm) followed by removal of the rod post-ligation. Sonographic images show the normal condition (top) and the partial occlusion status of the LCA (bottom) post ligation surgery; yellow arrows indicate the top and bottom points of ligation. B) Doppler ultrasound images show disturbed flow formation in the region distal to the ligation point of the LCA in contrast to unidirectional laminar flow in the normal and RCA groups; yellow arrows indicate the blood flow direction. C) Filamin A was highly expressed on the endothelial layer in the LCA compared to the RCA (white arrow). Scale bar = 100  $\mu\text{m}$ . Next, NVs were intravenously administered for systemic circulation on day 3 post porcine PCL surgery, followed by vessel harvest and analysis at day 21 post-injection. IVIS and immunostaining images of retrieved D,E) LCA and F,G) aortic arch (formation area of natural disturbed flow) samples showing effective PMSC-NV targeting of disturbed flow sites in the porcine model. The intensity of the targeted NV was quantified (right graphs). Scale bar = 50  $\mu\text{m}$ , 20  $\mu\text{m}$  for 400 $\times$  magnification and 1600 $\times$  magnification, respectively. \*\*\* $p < 0.001$  between comparison groups.

that the signals of PMSC-NVs increased under the disturbed flow condition (Figure 6F; Figure S15, Supporting Information) along with stronger colocalization with filamin A (Figure 6G) as compared to that observed under the normal flow condition, thereby validating the theragnostic potential of PMSC-NVs in a clinical setting.

### 3. Discussion

We previously demonstrated that PREY-conjugated liposomes exhibited effective targeting to ECs (CD31<sup>+</sup>) at the disturbed flow site, which was mediated through their uptake and

subsequent delivery by circulating immune cells (CD45<sup>+</sup>).<sup>[12]</sup> Our previous study has reported that PREY peptide sequence is homologous to myoferlin, and PREY-nanocarriers were preferentially bound to fibronectin and filamin A in vessels under disturbed flow.<sup>[12]</sup> The abnormal stress of disturbed blood flow triggered the overexpression of filamin A in the plasma membrane of ECs. As a mechanosensing protein,<sup>[24]</sup> filamin A interacts with caveolae and myoferlin,<sup>[12,25]</sup> and its function involves the maintenance of vascular homeostasis and EC junctions by triggering caveolin endocytosis.<sup>[26]</sup> Given the confirmation that PREY targets filamin A, PMSC-NVs appear to be able to specifically target ECs under a mechanosensing process of disturbed flow (“activated ECs”) and are subsequently internalized



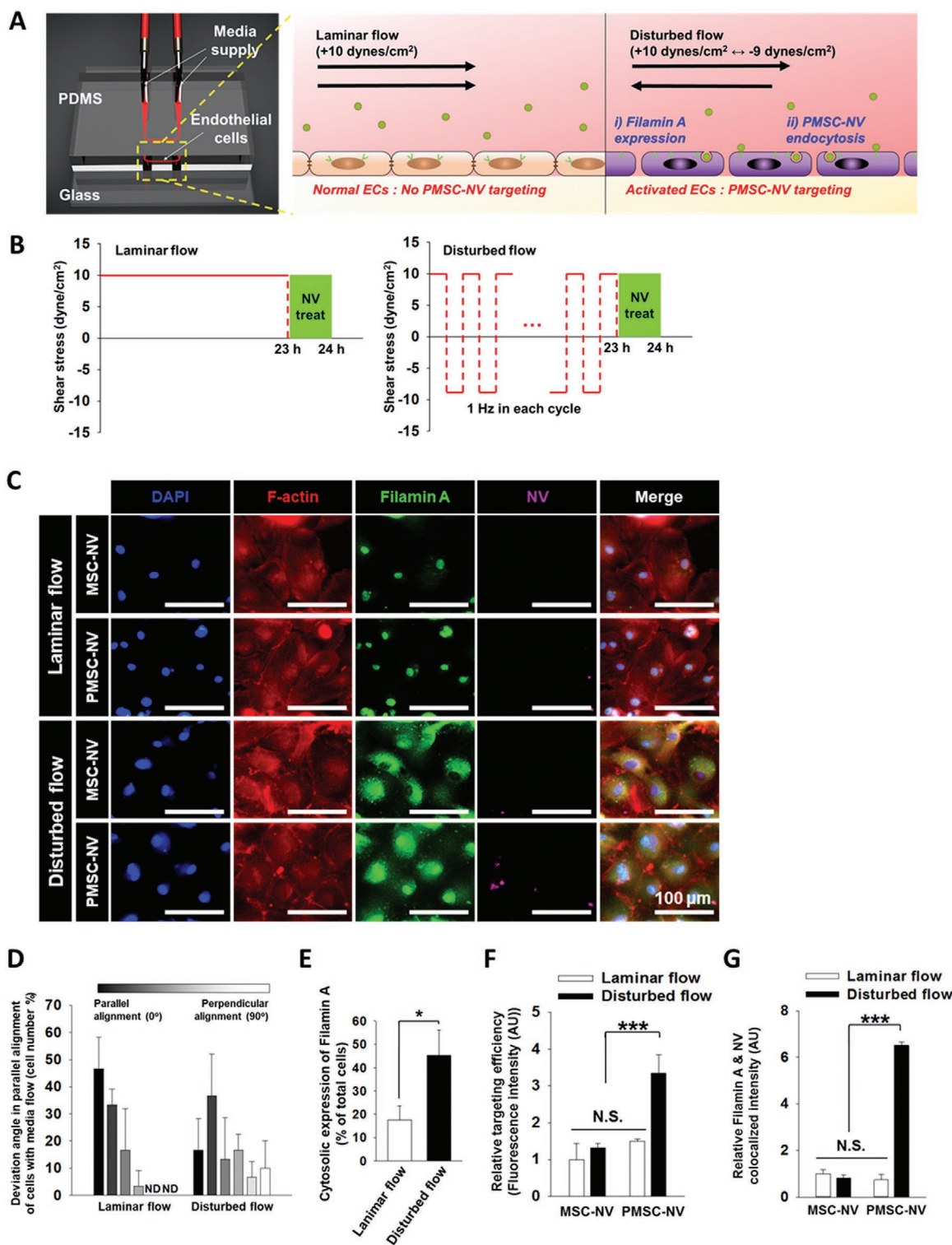


**Figure 6.** Efficiency of PMSC-NV targeting of human arterial ECs under disturbed flow in a microfluidic model. A) Human carotid artery endothelial cells (hCAECs) were cultured under unidirectional laminar or disturbed flow for 1 day at 12 h after cell seeding and then treated with NV for 1 h. B) Normal (laminar) flow and disturbed flow patterns represented as plots. C) Alignment of hCAECs as well as filamin A expression determined by immunostaining of F-actin (red) and filamin A (green) (blue: nucleus with DAPI staining). D) F-actin alignment with the flow direction and E) cytosolic filamin A expression under disturbed flow were quantitatively determined. F) In vitro efficiency of MSC-NV and PMSC-NV targeting of hCAECs in disturbed flow sites were determined by measuring the NV fluorescence intensity. G) Co-localization of filamin A with NVs was determined by immunostaining, thereby verifying the PREY targeting of filamin A. N.D. indicates non detectable. N.S. indicates no significant difference between the groups. \*\*\* $p < 0.001$  between/among comparison groups.



through caveolin-mediated endocytosis. Moreover, the presence of filamin A expression in the neointimal lesion (Figure 4C) as well as in VSMCs<sup>[27]</sup> suggests VSMCs as another potential candidate for PREY targeting because these cells could migrate into the neointima upon atherogenic activation. The MSC-conditioned media contained exosomes and was reported to suppress VSMC proliferation in injured arteries,<sup>[28]</sup> further supporting the PMSC-NV-mediated suppression of VSMC activation observed in the present study.

MSC-NVs were chosen for this design because i) their cell membrane-like properties at a nanoscale can prolong the systemic circulation time and thereby enhance endocytosis or membrane fusion-mediated intracellular delivery; ii) MSC-derived components reduce inflammatory<sup>[7b]</sup>/EC-dysfunctional activities<sup>[29]</sup> and avoid host immune rejection, thereby supporting their potential as therapeutic and delivery vehicles, respectively; iii) concern regarding the possible differentiation of MSCs into VSMCs<sup>[30]</sup> (a major mediator of neointimal formation) can be avoided using NVs (a nonvital cell derivative); and iv) NVs preserve the PREY transfection signature from MSCs and can be more easily produced on a large scale compared to exosomes.

Recently, miRNA delivery through exosomes has been studied in pathophysiological contexts.<sup>[31]</sup> Here, we focused on the comparison of miRNA profiles among PMSC-NVs, MSC-NVs, and PMSC as internal components, owing to their abundance in exosomes<sup>[32]</sup> and reported anti-atherogenic paracrine effect.<sup>[33]</sup> MSC-derived exosomes<sup>[34]</sup> contain miRNAs with anti-inflammatory (miR-21,<sup>[35]</sup> miR-let7,<sup>[34]</sup> miR-126,<sup>[36]</sup> miR-145,<sup>[37]</sup> and miR-146<sup>[38]</sup>), pro-EC recovery (miR-126<sup>[39]</sup> and miR-146<sup>[40]</sup>), and anti-VSMC activation (miR-143<sup>[32]</sup> and miR-145<sup>[32,37]</sup>) miRNAs. The internal components of NVs were preserved in a significant degree from the corresponding hMSC source (Figure 11). The result of miRNA array indicated that the extrusion processes altered miRNA contents more than twofold differences (PMSC versus PMSC-NV) in only 6.71% of the total miRNAs. This small difference might affect the therapeutic effect of PMSC-NVs compared to PMSCs. However, among the exosomal anti-atherogenic miRNAs, the levels of miR-21, miR-146, miR-143, and let-7 increased during the PMSC-NV production process, which is likely owing to volumetric concentration, supporting the use of non-vital products over the corresponding cell source. On the other hand, expression of only 3.3% miRNAs (86 out of 2578) reduced more than twofold in PMSC-NV compared to PMSC, which might also affect the therapeutic effect. In a current follow-up study to analyze the mRNA profile further, overexpression of the up- or downregulated miRNAs is conducted to optimize the therapeutic effects and thereby to engineer more potent NVs.

As an immunosuppressant, cyclosporin A (CyA) inhibits one of the key angiogenic mechanisms, nuclear factor of activated-T cells (NAFT) signaling in ECs through formation of CyA-CuPA complex and its binding to cytoplasmic phosphatase calcineurin. This process consequently inhibits phosphorylation of NAFT and its subsequent nuclear translocation, thereby inducing pro-inflammation. As a result, pro-angiogenic gene expression, proliferation, tube formation, and sprouting of ECs are dysregulated.<sup>[41]</sup> Previous studies reported that miR-126<sup>[42]</sup> and miR-146<sup>[40]</sup> exerted therapeutic effects to promote angiogenesis of dysfunctional ECs. Since MSC-NVs contain

these genes, their therapeutic effects appeared to promote EC-recovery under CyA treatment (Figure 3E).

Despite species mismatch, human stem cell-derived NVs were used in the two animal models, because of a need to test the therapeutic effect of NVs from a small animal model to a large one and further to a human cell model. Mouse, pig, or human stem cell-derived NVs could be used in each of species-matched experimental model. However, since the final goal of this development is translation of PREY-NVs for not saving animals but human clinic, human stem cell-derived NVs were chosen to test in the three models. The in vivo immunogenic response to xenogenic MSC source is very controversial in current academic circles. One opinion is that MSCs are immune evasive to allogenic and xenogenic recipients,<sup>[43]</sup> while the other indicates that allogenic and xenogenic MSCs have therapeutic effect without immunosuppressant.<sup>[44]</sup> In our study, hMSC-NVs did not exert any immune evasive effect in the mouse and pig models, indicating a need of future study on the subject for validation. Second, the choice of animal models was based on not atherosclerosis but disturbed blood flow<sup>[45]</sup> as PREY was screened and selected in mouse PCL model.<sup>[12]</sup> Therefore, even though a human atherosclerosis model may be available, testing in the mouse and porcine model<sup>[21]</sup> of disturbed flow was inevitable due to no clear human model of disturbed flow.

It has been reported that the circulation half-life of the exosomes is 30 min and can be completely cleared from the circulation in vivo in 6 h after IV injection.<sup>[46]</sup> Considering the fact hMSC-NV have similar size, structure, and components to exosome in nature, it was assumed that the in vivo kinetics should not be too different between them. As a follow-up development, chemical conjugation of PREY for the outward membrane display is being currently optimized. Therefore, after this step is done, further studies are needed to validate the in vivo kinetics, since other factors (e.g., PREY amount, membrane mechanics, particle-particle adhesion, etc) can affect the circulation.

## 4. Conclusion

In summary, this study offers an unprecedented solution to a long-standing issue in anti-atherosclerosis therapy by demonstrating the potent theragnostic function of PMSC-NVs, which could prevent the development of atherogenesis in mouse and porcine PCL models as well as in a microfluidic disturbed flow model with human coronary artery-derived ECs. This theragnostic effect was exerted by the synergistic function of PREY-mediated targeting to the earliest atherogenic event and MSC-derived therapeutic properties. Moreover, the PREY-plasmid design was unique in that the intended outward display and expression levels were achieved. The PREY-targeting ability was validated in not only multiple models but also in both artificial (PCL) and natural disturbed flow (aortic arch) sites. These promising results suggest PMSC-NVs as a potential next-generation platform for translational medicine.

## 5. Experimental Section

*Plasmid Design and Cloning for PREY Expression:* The plasmid used to express and localize PREY outward on the cell membrane consisted

of an outward N-terminal-promoter-signal peptide-PREY-V5-TMP-GFP-inward C-terminal structure. In the plasmid sequence, the signal peptide guided localization of the PREY peptide outside the cell membrane, and the V5 tag and GFP were added to monitor the location and expression level of PREY. The expression vectors were cloned using an NEB Gibson Assembly kit (New England Biolabs, MA, USA) following the manufacturer's instructions. Signal peptides and each type of TMP were separately amplified by PCR using the following templates: BKU002587 and BKU008396 (Korea Human Gene Bank, Republic of Korea), and NGFR (Addgene plasmid #27489; Addgene, MA) for CD86, CD105, and the truncated CD271 ( $\Delta$ LNGFR).<sup>[47]</sup> The vector components were inserted into a Cas9-digested p3S-Cas9-HN (Addgene plasmid #104171) backbone with plasmid synthesis (Macrogen, Republic of Korea). Following this procedure, PCR amplification and Gibson cloning were performed. All primers and plasmid sequences are listed in Tables S3 and S4, Supporting Information.

**Determination of Transfection Efficiency:** The efficiency of PREY transfection was compared among the test candidates of TMPs (CD86, CD105, and CD271) in combination with two MSC types (ASC and BMSC) at day 1 post-transfection by flow cytometry with quantitative analysis using FACSCanto (BD Bioscience, CA, USA). The cells were immunostained with an anti-v5tag primary antibody (ab27671, Abcam, MA, USA) and Alexa Fluor 647-conjugated secondary antibody (Jackson Immuno Research, PA, USA). To evaluate plasmid dose-dependent apoptosis, transfected ASCs and BMSCs were harvested at 30 min after transfection, immunostained with Alexa Fluor 488-conjugated annexin V (Thermo Fisher Scientific, CA, USA), and subjected to flow cytometry analysis. The viable cell number was also counted by trypan blue staining at day 1 post-transfection.

**NV Extrusion:** Experiments with human subjects were carried out with the full, informed consent of the subjects, in accordance with all local laws and with the approval of all relevant ethics bodies. A well-established NV extrusion method was used as previously reported.<sup>[13,48]</sup> At day 3 post-transfection, human ASCs (Promocell, Germany), BMSCs (Lonza, Switzerland), and PMSCs were washed twice using phosphate-buffered saline (PBS) and detached using 0.25% trypsin/EDTA. To produce NVs, the cell suspensions in PBS ( $1 \times 10^6$  cells mL<sup>-1</sup>) were extruded six times with 10- $\mu$ m, 5- $\mu$ m, and 400-nm pore-sized polycarbonate membrane filters (Whatman, UK) in sequence using an extruder kit (Avanti Polar Lipids, AL, USA). After serial extrusion steps with the 10 and 5- $\mu$ m membrane filters, the NVs were collected by centrifuging at 15 000 g for 30 min, and intact NV formation around a 100-nm diameter range without centrifugation-mediated destructive effects was confirmed as shown in previous studies.<sup>[13,48]</sup> The centrifugation step was immediately performed after extrusion to remove the surrounding buffer, thereby preventing the loss of internal RNAs through exchange with the buffer. Next, the pellet was re-suspended in PBS and the aggregated NVs were filtered out using a 0.2- $\mu$ m syringe filter (Avantec, Japan). The 400-nm filter was used for the last extrusion step to produce NVs below 100 nm with a low polydispersity index, which were stored at -70 °C until use. The sizes and morphologies of the PMSC-NVs were determined by TEM (JEM-F200, JEOL, Japan).

The outward display of PREY on PMSC-NV was evaluated by confocal imaging (LSM780, Zeiss) after immunostaining for the v5 tag using Alexa Fluor 594-conjugated secondary antibody (Jackson Immune Research, PA, USA) as well as by TEM imaging after staining with gold (10 nm)-conjugated secondary antibody (Abcam). Confocal z-stack image slices were merged using ZEN imaging software (ZEN 2012, Zeiss). The result was double-checked by measuring the zeta potential (ELS-1000ZS, Otsuka Electronics, Japan) of PMSCs and PMSC-NVs.

**Mouse PCL Model:** All animal studies were carried out by procedures approved by the Institutional Animal Care and Use Committee (IACUC) of Yonsei University College of Medicine (2018-0044). The surgical procedure was performed with 6-week-old male Balb/c (Orient Bio Inc., Republic of Korea) or KOR-ApoE (shl) (SLC, Japan) mice. For the PCL surgery, anesthesia was applied by intraperitoneal injection of xylazine (10 mg kg<sup>-1</sup>) and zoletil (50 mg kg<sup>-1</sup>) mixture. The neck was shaved and disinfected using betadine, and then a midline incision was made

(5 mm). After exposure of the LCA, three of the four branches of the LCA (ECA, ICA, OA) were ligated with a 10-0 polyamide suture, leaving the STA unligated, and the incisions were closed with 6-0 silk sutures. The mice were then monitored and fed an atherogenic diet (Research Diets, NJ, USA), and MSC-NVs, PMSCs, or PMSC-NVs were intravenously administered at day 3 post-ligation.

**Determination of Targeting Efficiency and Anti-Atherogenic Effect in the Mouse PCL Model:** The in vivo efficiency of PMSC-NV targeting disturbed flow sites was determined in the mouse PCL model by IVIS imaging (PerkinElmer, WA, USA) and histology at 24 h after injection of the test groups. The ASCs were labeled with VivoTrack 680 (PerkinElmer) for 30 min before NV extrusion, and the free dye was completely removed by multiple centrifugation steps, thereby preventing micelle formation of dyes, followed by NV extrusion. The labeled cells and NVs were intravenously injected into the PCL mice and IVIS imaging was conducted under breath anesthetization with isoflurane. The mice were then sacrificed, and their LCAs, RCAs, and major organs were harvested for ex vivo IVIS imaging and histology. Tissue sections of the LCAs and RCAs were immunostained with anti-filamin A antibody (ab51217, Abcam), and the corresponding fluorescence intensity was quantified using ImageJ software. Tissue sections were also stained with H&E and Masson's trichrome, or immunostained with anti-CD68 antibody (ab125212, Abcam) and anti-VCAM-1 antibody (ab134047, Abcam). The neointima structure factors (area ratio of neointima to neointima+ lumen, area ratio of neointima to media, and neointima area) or the corresponding fluorescence intensities were quantitatively analyzed using ImageJ.

**Determination of Targeting Efficiency in the Porcine PCL Model:** The PCL surgery was performed on female Yorkshire pigs with a mass of 25–30 kg (XP Bio, Republic of Korea) following a previous study.<sup>[21]</sup> The animal studies were approved by the IACUC of Yonsei University College of Medicine (2017-0058). The pigs were subjected to an intramuscular injection of atropine (0.04 mg kg<sup>-1</sup>), xylazine (2 mg kg<sup>-1</sup>), and azaperone (2 mg kg<sup>-1</sup>) in mixture as a premedication. The pigs were then anesthetized with Alfaxan (1 mg kg<sup>-1</sup>) and maintained in this state by endotracheal intubation of 2% isoflurane during surgery. The neck was disinfected using betadine and then a midline skin incision was made. A sterilized stainless-steel rod (outer diameter = 0.9 mm) was placed as a spacer on the LCA and ligated together with a 5-0 silk suture (Figure 5A). The rod was sequentially removed, and the incision was closed by suturing, resulting in an 80% occlusion of the carotid artery. The RCA was left without ligation as a normal control group. The blood flow pattern was observed by sonography (S22V; SonoScape Medical Corp., China). Vivotrack680-labeled MSC-NVs or PMSC-NVs were intravenously injected via an ear vein (1 mg per pig) on day 3 post-ligation, and the pigs were sacrificed at 24 h or 21 days post-injection. The RCAs, LCAs, and aortic arches were retrieved for ex vivo IVIS and histology analysis. Their tissue sections were immunostained with anti-filamin A antibody and anti-CD31 antibody (sc-1506, Santa Cruz Biotechnology, CA, USA), followed by fluorescence imaging and ImageJ analysis.

**Determination of Targeting Efficiency on Human ECs in an In Vitro Flow Model:** As previously described,<sup>[49]</sup> microfluidic devices were produced with polydimethylsiloxane (Dow Corning, MI, USA) by soft lithography, bonded with glass coverslips (VWR, PA, USA), and placed in polystyrene boxes (Ted Pella Inc., CA, USA). The devices were sterilized with 70% ethanol and washed with PBS. The channels were then coated with 50  $\mu$ g mL<sup>-1</sup> of collagen I (Corning, MA, USA) at 37 °C for 1 h. hCAECs (Lonza) or hAECs (Lonza) were seeded ( $2 \times 10^7$  cells mL<sup>-1</sup>) into the channel for 12 h. The outlet of each device was connected to PHD ULTRA syringe pumps (Harvard Apparatus, MA, USA) to create normal and disturbed media flow. To generate normal laminar flow, the medium was perfused at 22.5  $\mu$ L min<sup>-1</sup> with a shear stress of 10 dyne cm<sup>-2</sup>. Disturbed flow was generated by repeated cycles of injecting and withdrawing the medium at a flow rate of 22.5  $\mu$ L min<sup>-1</sup> (10 dyne cm<sup>-2</sup>) and 20  $\mu$ L min<sup>-1</sup> (9 dyne cm<sup>-2</sup>), respectively. After the human ECs were exposed to either flow type, NVs (10  $\mu$ g mL<sup>-1</sup>) were perfused into the channels at 37 °C for 1 h. The orientation of the cell compared to the flow direction was quantitatively determined by analyzing each cell in the acquired images ( $N = 30$ –35 cells) using ImageJ. NV uptake into

ECs and its co-localization with filamin A in each test group was also quantitatively analyzed using ImageJ.

**qRT-PCR and miRNA Array:** Total RNA was extracted from each sample using 1 mL TRIzol reagent (Invitrogen) according to the manufacturer's instructions. The RNA was dissolved in diethyl pyrocarbonate water, and cDNA was synthesized using AccuPower CycleScript RT PreMix (Bioneer, Republic of Korea). PCR was performed with SYBR Green PCR mix (Thermo Fisher Scientific) in a StepOnePlus real-time PCR system (Applied Biosystems, CA, USA). Glyceraldehyde 3-phosphate dehydrogenase served as a housekeeping gene, and the gene expression level of each marker was determined using the relative quantification method ( $2^{-\Delta\Delta Ct}$ ). The primer sequences are listed in Table S5, Supporting Information. The dissolved RNA was profiled using miRNA array (GeneChip 4.0 microRNA Microarray; Affymetrix, Japan) following the manufacturer's instructions.

**Immunofluorescence Staining of Cells and Tissues:** Cell samples were fixed with 4% paraformaldehyde (Sigma-Aldrich) for 10 min, while tissue samples were fixed with 10% paraformaldehyde for 3 days, and both were performed at room temperature. The fixed samples were washed with PBS twice and embedded in paraffin to make tissue sections. The sections were then hydrated using a series of xylene and ethanol solutions (100%, 95%, 80%, and 70% v/v in deionized water) and treated with a pepsin reagent (Sigma-Aldrich) for 30 min at 37 °C for antigen retrieval. Next, the tissue sections were treated with a blocking solution (5% bovine serum albumin [Millipore, MD] + 0.3% triton X-100 [Sigma-Aldrich]) for 1 h at room temperature. The primary antibodies were anti-v5 tag antibody (ab27671, Abcam), anti-VCAM-1 (ab134047, Abcam), anti-CD68 (ab125212, Abcam), anti-Filamin A (ab51217, Abcam), and anti-CD31 (sc-1506, Santa Cruz Biotechnology, CA, USA). These antibodies were treated in PBS with 1:100 dilutions, followed by treatment of the corresponding secondary antibodies in PBS with 1:200 dilutions. The secondary antibodies were anti-mouse conjugated to Alexa Fluor 594, anti-rabbit conjugated to Alexa Fluor 594, anti-rabbit conjugated to Alexa Fluor 488, and anti-goat conjugated to Alexa Fluor 488 (all from Jackson Laboratories). The samples were then mounted and counterstained with a mounting solution containing 4',6-diamidino-2-phenylindole (DAPI, Vector Laboratories, CA, USA) to visualize the cell nuclei.

**Western Blot Analysis:** Samples were lysed with RIPA buffer (Sigma-Aldrich) to obtain total proteins, whose concentrations were determined using a Bradford assay (Sigma-Aldrich). Protein extracts were run on a 10% (w/v) sodium dodecyl sulfate-polyacrylamide gel electrophoresis gel and then electrotransferred onto a nitrocellulose membrane. The membranes were blocked in TBST (20 mM Tris, 0.9% NaCl, 0.1% Tween 20, pH 7.4) with 5% (w/v) skim milk and then incubated with the primary antibodies anti-v5 tag (ab27671, Abcam), anti-GFP (ab32146, Abcam), anti-CD9 (ab92726, Abcam), and anti- $\beta$ -actin (ab8227, Abcam). The secondary antibodies, goat anti-mouse IgG (H+L)-HRP conjugated and goat anti-rabbit IgG (H+L)-HRP conjugated antibodies (all from Vector Laboratories), were then applied according to the manufacturer's instructions. The signals were visualized using the CL Plus Western Blotting Detection kit (Amersham Biosciences, UK) according to the manufacturer's instructions and analyzed using the LAS-3000 image reader (Fujifilm, Japan).

**Statistical Analysis:** Descriptive statistics were used to determine group means and standard deviations. Statistical comparisons were made using two-way analysis of variance (ANOVA) with Tukey's post-hoc analysis when groups were compared with respect to one measurement variable and two nominal variables (factors), or one-way ANOVA when two or more groups were compared with respect to one measurement variable and one nominal variable (factor). When only two groups were compared, the two-sample *t*-test was used (SigmaPlot 12.0, Systat Software, Inc., CA, USA). *p* values < 0.05 were considered to indicate minimum statistical significance.

## Supporting Information

Supporting Information is available from the Wiley Online Library or from the author.

## Acknowledgements

J.-K.Y., D.-H.K., and M.-L.K. contributed equally to this work. This study was supported by the Basic Science Research Program through the National Research Foundation of Korea (NRF) funded by the Ministry of Science, ICT, and Future Planning (NRF-2016M3A9E9941743; H.J.S.), Ministry of Education (NRF-2018R1A6A3A01012997; J.K.Y.), the American Heart Association Scientist Development Grant 15SDG25080314 (Y.K.), and the National Institutes of Health Director's New Innovator Award 1DP2HL142050 (Y.K.). This work was partially performed at the core facilities at the Parker H. Petit Institute for Bioengineering and Bioscience at the Georgia Institute of Technology and the Institute for Electronics and Nanotechnology at the Georgia Institute of Technology, a member of the National Nanotechnology Coordinated Infrastructure, which is supported by the National Science Foundation (Grant ECCS1542174).

## Conflict of Interest

The authors declare no conflict of interest.

## Keywords

atherosclerosis, disturbed blood flow, mesenchymal stem cells, nanovesicles, plasmid design

Received: January 1, 2020

Revised: February 28, 2020

Published online: April 2, 2020

- [1] K. S. Cunningham, A. I. Gotlieb, *Lab. Invest.* **2005**, *85*, 9.
- [2] a) Y. S. Chatzizisis, A. U. Coskun, M. Jonas, E. R. Edelman, C. L. Feldman, P. H. Stone, *J. Am. Coll. Cardiol.* **2007**, *49*, 2379; b) M. A. Gimbrone Jr., G. Garcia-Cardena, *Circ. Res.* **2016**, *118*, 620.
- [3] C. Hahn, M. A. Schwartz, *Nat. Rev. Mol. Cell Biol.* **2009**, *10*, 53.
- [4] U. Landmesser, B. Hornig, H. Drexler, *Circulation* **2004**, *109*, 1127.
- [5] a) X. Zhang, F. Huang, Y. Chen, X. Qian, S. G. Zheng, *Am. J. Transl. Res.* **2016**, *8*, 4017; b) F. Li, X. Guo, S. Y. Chen, *Front. Cardiovasc. Med.* **2017**, *4*, 32; c) V. Frodermann, J. van Duijn, M. van Pel, P. J. van Santbrink, I. Bot, J. Kuiper, S. C. de Jager, *Sci. Rep.* **2015**, *5*, 15559.
- [6] R. W. Yeo, R. C. Lai, B. Zhang, S. S. Tan, Y. Yin, B. J. Teh, S. K. Lim, *Adv. Drug Delivery Rev.* **2013**, *65*, 336.
- [7] a) R. C. Lai, T. S. Chen, S. K. Lim, *Regener. Med.* **2011**, *6*, 481; b) X. Teng, L. Chen, W. Chen, J. Yang, Z. Yang, Z. Shen, *Cell. Physiol. Biochem.* **2015**, *37*, 2415.
- [8] Y. Zhou, H. Xu, W. Xu, B. Wang, H. Wu, Y. Tao, B. Zhang, M. Wang, F. Mao, Y. Yan, S. Gao, H. Gu, W. Zhu, H. Qian, *Stem Cell Res. Ther.* **2013**, *4*, 34.
- [9] T. Li, Y. Yan, B. Wang, H. Qian, X. Zhang, L. Shen, M. Wang, Y. Zhou, W. Zhu, W. Li, W. Xu, *Stem Cells Dev.* **2013**, *22*, 845.
- [10] A. Mahmood, D. Lu, M. Chopp, *J. Neurotrauma* **2004**, *21*, 33.
- [11] S. C. Jang, O. Y. Kim, C. M. Yoon, D. S. Choi, T. Y. Roh, J. Park, J. Nilsson, J. Lotvall, Y. K. Kim, Y. S. Gho, *ACS Nano* **2013**, *7*, 7698.
- [12] L. H. Hofmeister, S. H. Lee, A. E. Norlander, K. R. Montaniel, W. Chen, D. G. Harrison, H. J. Sung, *ACS Nano* **2015**, *9*, 4435.
- [13] W. Jo, J. Kim, J. Yoon, D. Jeong, S. Cho, H. Jeong, Y. J. Yoon, S. C. Kim, Y. S. Gho, J. Park, *Nanoscale* **2014**, *6*, 12056.
- [14] N. Kosaka, H. Iguchi, Y. Yoshioka, F. Takeshita, Y. Matsuki, T. Ochiya, *J. Biol. Chem.* **2010**, *285*, 17442.
- [15] M. Simons, G. Raposo, *Curr. Opin. Cell Biol.* **2009**, *21*, 575.



- [16] a) D. M. Schrijvers, G. R. De Meyer, A. G. Herman, W. Martinet, *Cardiovasc. Res.* **2007**, *73*, 470; b) A. G. Suits, A. Chait, M. Aviram, J. W. Heinecke, *Proc. Natl. Acad. Sci. U. S. A.* **1989**, *86*, 2713.
- [17] W. C. Aird, *Blood* **2003**, *101*, 3765.
- [18] M. I. Cybulsky, K. Iiyama, H. Li, S. Zhu, M. Chen, M. Iiyama, V. Davis, J.-C. Gutierrez-Ramos, P. W. Connelly, D. S. Milstone, *J. Clin. Invest.* **2001**, *107*, 1255.
- [19] C. Wilasrusmee, M. Da Silva, B. Singh, S. Kittur, J. Siddiqui, D. Bruch, S. Wilasrusmee, D. S. Kittur, *J. Surg. Res.* **2002**, *104*, 131.
- [20] U. M. Fischer, M. T. Harting, F. Jimenez, W. O. Monzon-Posadas, H. Xue, S. I. Savitz, G. A. Laine, C. S. Cox Jr., *Stem Cells Dev.* **2009**, *18*, 683.
- [21] A. Ishii, F. Vinuela, Y. Murayama, I. Yuki, Y. L. Nien, D. T. Yeh, H. V. Vinters, *AJNR Am. J. Neuroradiol.* **2006**, *27*, 1893.
- [22] H. Miao, Y. L. Hu, Y. T. Shiu, S. Yuan, Y. Zhao, R. Kaunas, Y. Wang, G. Jin, S. Usami, S. Chien, *J. Vasc. Res.* **2005**, *42*, 77.
- [23] F. Robicsek, P. W. Sanger, F. H. Taylor, R. Magistro, E. Foti, *Ann. Surg.* **1958**, *147*, 835.
- [24] a) S. Huelsmann, N. Rintanen, R. Sethi, N. H. Brown, J. Ylanne, *Sci. Rep.* **2016**, *6*, 32798; b) Y. Shifrin, P. D. Arora, Y. Ohta, D. A. Calderwood, C. A. McCulloch, *Mol. Biol. Cell* **2009**, *20*, 1269.
- [25] M. Stahlhut, B. van Deurs, *Mol. Biol. Cell* **2000**, *11*, 325.
- [26] a) M. Sverdlov, V. Shinin, A. T. Place, M. Castellon, R. D. Minshall, *Mol. Biol. Cell* **2009**, *20*, 4531; b) G. S. Griffiths, M. Grundl, J. S. Allen III, M. L. Matter, *J. Cell. Physiol.* **2011**, *226*, 2287.
- [27] J. V. Small, D. O. Furst, J. de Mey, *J. Cell Biol.* **1986**, *102*, 210.
- [28] Y. Iso, S. Usui, M. Toyoda, J. L. Spees, A. Umezawa, H. Suzuki, *Biochem. Biophys. Rep.* **2018**, *16*, 79.
- [29] A. Forte, M. Finicelli, M. Mattia, L. Berrino, F. Rossi, M. de Feo, M. Cotrufo, M. Cipollaro, A. Cascino, U. Galderisi, *J. Cell. Physiol.* **2008**, *217*, 789.
- [30] Y. Li, J. Yu, M. Li, Z. Qu, Q. Ruan, *Life Sci.* **2011**, *88*, 130.
- [31] M. Tomasetti, W. Lee, L. Santarelli, J. Neuzil, *Exp. Mol. Med.* **2017**, *49*, e285.
- [32] K. R. Cordes, N. T. Sheehy, M. P. White, E. C. Berry, S. U. Morton, A. N. Muth, T. H. Lee, J. M. Miano, K. N. Ivey, D. Srivastava, *Nature* **2009**, *460*, 705.
- [33] M. W. Feinberg, K. J. Moore, *Circ. Res.* **2016**, *118*, 703.
- [34] J. Li, H. Xue, T. Li, X. Chu, D. Xin, Y. Xiong, W. Qiu, X. Gao, M. Qian, J. Xu, Z. Wang, G. Li, *Biochem. Biophys. Res. Comm.* **2019**, *510*, 565.
- [35] A. Canfran-Duque, N. Rotllan, X. Zhang, M. Fernandez-Fuertes, C. Ramirez-Hidalgo, E. Araldi, L. Daimiel, R. Busto, C. Fernandez-Hernando, Y. Suarez, *EMBO Mol. Med.* **2017**, *9*, 1244.
- [36] Y. Wu, L. T. Song, J. S. Li, D. W. Zhu, S. Y. Jiang, J. Y. Deng, *J. Periodontol.* **2017**, *88*, e179.
- [37] X. Guo, L. Yu, M. Chen, T. Wu, X. Peng, R. Guo, B. Zhang, *J. Transl. Med.* **2016**, *14*, 211.
- [38] J. Xu, W. Wu, L. Zhang, W. Dorset-Martin, M. W. Morris, M. E. Mitchell, K. W. Liechty, *Diabetes* **2012**, *61*, 2906.
- [39] a) Y. Suarez, W. C. Sessa, *Circ. Res.* **2009**, *104*, 442; b) T. A. Harris, M. Yamakuchi, M. Ferlito, J. T. Mendell, C. J. Lowenstein, *Proc. Natl. Acad. Sci. U. S. A.* **2008**, *105*, 1516.
- [40] H. S. Cheng, N. Sivachandran, A. Lau, E. Boudreau, J. L. Zhao, D. Baltimore, P. Delgado-Olguin, M. I. Cybulsky, J. E. Fish, *EMBO Mol. Med.* **2013**, *5*, 1017.
- [41] a) B. A. Nacev, J. O. Liu, *PLoS One* **2011**, *6*, e24793; b) B. A. Nacev, W. K. Low, Z. Huang, T. T. Su, Z. Su, H. Alkuraya, D. Kasuga, W. Sun, M. Trager, M. Braun, G. Fischer, K. Zhang, J. O. Liu, *J. Pharmacol. Exp. Ther.* **2011**, *338*, 466; c) L. Qin, D. Zhao, X. Liu, J. A. Nagy, M. V. Hoang, L. F. Brown, H. F. Dvorak, H. Zeng, *Mol. Cancer Res.* **2006**, *4*, 811; d) M. Storogenko, M. A. Pech-Amsellem, S. Kerdine, F. Rousselet, M. Pallardy, *Life Sci.* **1997**, *60*, 1487.
- [42] Y. Suárez, W. C. Sessa, *Circ. Res.* **2009**, *104*, 442.
- [43] J. A. Ankrum, J. F. Ong, J. M. Karp, *Nat. Biotechnol.* **2014**, *32*, 252.
- [44] C. S. Lin, G. Lin, T. F. Lue, *Stem Cells Dev.* **2012**, *21*, 2770.
- [45] D. Nam, C. W. Ni, A. Rezvan, J. Suo, K. Budzyn, A. Llanos, D. Harrison, D. Giddens, H. Jo, *Am. J. Physiol.: Heart Circ. Physiol.* **2009**, *297*, H1535.
- [46] C. P. Lai, O. Mardini, M. Ericsson, S. Prabhakar, C. Maguire, J. W. Chen, B. A. Tannous, X. O. Breakefield, *ACS Nano* **2014**, *8*, 483.
- [47] R. O. Bak, D. P. Dever, M. H. Porteus, *Nat. Protoc.* **2018**, *13*, 358.
- [48] Y. W. Choo, M. Kang, H. Y. Kim, J. Han, S. Kang, J. R. Lee, G. J. Jeong, S. P. Kwon, S. Y. Song, S. Go, M. Jung, J. Hong, B. S. Kim, *ACS Nano* **2018**, *12*, 8977.
- [49] Y. J. Sei, S. I. Ahn, T. Virtue, T. Kim, Y. Kim, *Sci. Rep.* **2017**, *7*, 10019.